

# Mesoporous $\text{TiO}_2$ -Sn@C core-shell microspheres for Li-ion batteries†

Jizhang Chen,<sup>a</sup> Li Yang,<sup>\*ab</sup> Zhengxi Zhang,<sup>a</sup> Shaohua Fang<sup>a</sup> and Shin-ichi Hirano<sup>b</sup>

Cite this: *Chem. Commun.*, 2013, **49**, 2792

Received 26th January 2013,  
Accepted 15th February 2013

DOI: 10.1039/c3cc40671g

www.rsc.org/chemcomm

**Using amorphous  $\text{TiO}_2$  microspheres as precursors, we obtain mesoporous  $\text{TiO}_2$ -Sn@C core-shell microspheres. Sn is encapsulated into a  $\text{TiO}_2$  matrix, and carbon is coated outside. This intriguing architecture can effectively buffer volume change and structural stress, thus contributing to excellent long-term cycling stability and superior high-rate cyclability.**

With advantages such as high energy density, high safety, low cost, and long lifespan, lithium ion batteries (LIBs) have attracted significant research interest worldwide.<sup>1</sup> LIBs are considered as the most promising energy storage technologies for electrical vehicles, portable electronic devices, and renewable energy such as wind and solar.<sup>2</sup> Metallic tin (Sn) is one of the most promising anode materials for next-generation LIBs due to its high theoretical capacity of  $991 \text{ mA h g}^{-1}$  or  $7313 \text{ mA h cm}^{-3}$ , multiple times that of commercialized graphite anode materials ( $372 \text{ mA h g}^{-1}$  or  $833 \text{ mA h cm}^{-3}$ ).<sup>3</sup> In addition, the operating potential of Sn is slightly higher than that of graphite, not only providing a high voltage for a full cell, but also ensuring higher safety.<sup>4</sup> However, the huge volume expansion (up to 360%) and dramatic mechanical stress of Sn during cycling cause cracking and pulverization of the active material and loss of conductivity at the electrode, thus leading to quick capacity fading, which greatly hinders the practical application of Sn.<sup>5</sup> To overcome this obstacle, nanostructure has been employed to reduce the absolute volume expansion of Sn, whereas the cycling stability is still far from satisfaction.<sup>6</sup> In fact, nanosized Sn suffers from aggregation in both fabrication and cycling processes. To address this problem, a second phase has to be introduced to prevent the aggregation of Sn into large grains and function as a cushion to buffer volume change and structural stress of Sn. Usually, embedding Sn into a carbon matrix is an effective strategy to improve the cycling stability,<sup>7</sup> since carbon is highly conductive, elastic and flexible.

Another anode material anatase  $\text{TiO}_2$  experiences negligible volume change ( $<4\%$ ) upon  $\text{Li}^+$  intercalation and de-intercalation, which contributes to great structural stability and long cycle life.<sup>8</sup> The disadvantages of  $\text{TiO}_2$  are its low conductivity and low theoretical capacity ( $168.5 \text{ mA h g}^{-1}$ ). Considering that Sn and  $\text{TiO}_2$  anode materials possess complementary characteristics, here we prepare Sn- $\text{TiO}_2$  composites, trying to combine their merits. Mesoporous structure and a carbon shell are also introduced so as to suppress cracking or pulverization of the active material. Our final product is mesoporous  $\text{TiO}_2$ -Sn@C core-shell microspheres, which exhibit a reversible capacity of  $206.2 \text{ mA h g}^{-1}$  at  $500 \text{ mA g}^{-1}$  after 2000 cycles. Such a long term cycling stability has never been reported for Sn anode materials. This composite also gives a superior rate performance of  $131.8 \text{ mA h g}^{-1}$  at  $5000 \text{ mA g}^{-1}$ , 5.8 times that of typical graphite anode materials.

Fig. 1 describes the fabrication process, using amorphous  $\text{TiO}_2$  as the precursor. This precursor possesses the morphology of mono-dispersed microspheres with a smooth surface. The diameter is between 150 and 400 nm, as shown in Fig. 2a. After step I, hydrothermal reaction, pure crystallized anatase  $\text{TiO}_2$  (Fig. S1, ESI†) would be obtained if a tin source ( $\text{K}_2\text{SnO}_3$ ) is not added. In this situation, mesoporous  $\text{TiO}_2$  microspheres (Fig. S2a, ESI†) are obtained after 3 h reaction. After 12 h, the  $\text{TiO}_2$  microspheres collapse and turn out to be dispersed small particles (Fig. S2b, ESI†), due to an effect similar to the Kirkendall effect. In alkaline solution at high temperature and high pressure, amorphous  $\text{TiO}_2$  is etched by  $\text{OH}^-$ , forming  $\text{HTiO}_3^{3-}$  anions.  $\text{HTiO}_3^{3-}$  anions then diffuse

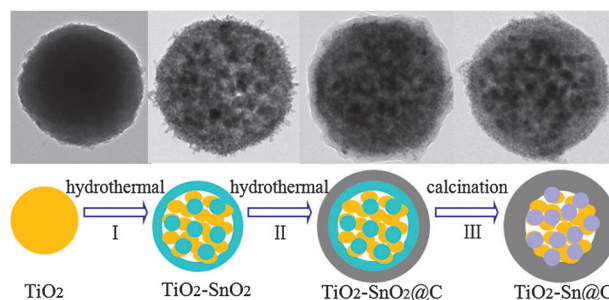
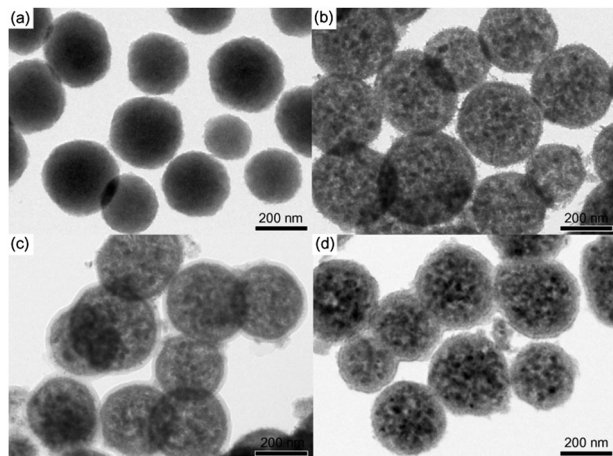


Fig. 1 Schematic illustration of the fabrication process.

<sup>a</sup> School of Chemistry and Chemical Engineering, Shanghai Jiaotong University, Shanghai 20024, P.R. China. E-mail: liyangce@sjtu.edu.cn

<sup>b</sup> Hirano Institute for Materials Innovation, Shanghai Jiaotong University, Shanghai 200240, China

† Electronic supplementary information (ESI) available: Experimental details, schematic illustration, TEM images, SEM images, XRD patterns, Raman spectra,  $\text{N}_2$  adsorption and desorption isotherms and initial three discharge-charge curves. See DOI: 10.1039/c3cc40671g



**Fig. 2** TEM images (a)  $\text{TiO}_2$  precursor, (b)  $\text{TiO}_2\text{-SnO}_2$ , (c)  $\text{TiO}_2\text{-SnO}_2\text{@C}$ , and (d)  $\text{TiO}_2\text{-Sn@C}$ .

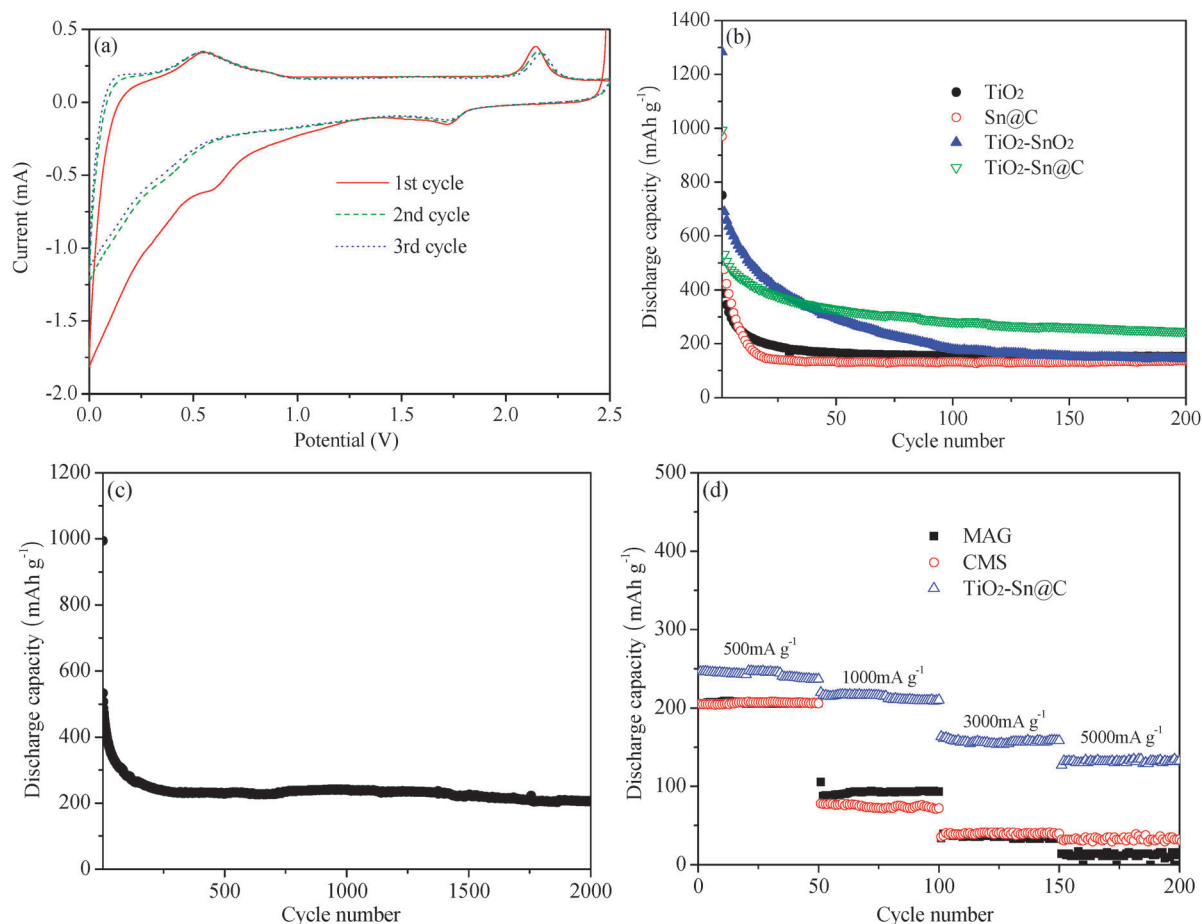
outside, form  $\text{H}_2\text{TiO}_3$  in the diffusion process, and transform into crystallized anatase  $\text{TiO}_2$ , which would collapse if the reaction time is long. If a  $\text{TiO}_2$  precursor is not involved in step I, pure  $\text{SnO}_2$  microspheres (Fig. S2c, ESI<sup>†</sup>) are obtained. When both  $\text{TiO}_2$  and  $\text{K}_2\text{SnO}_3$  are added,  $\text{SnO}_2$  is generated during the Kirkendall process (*i.e.* etching and re-crystallization) of  $\text{TiO}_2$ , inserted into and coat  $\text{TiO}_2$  mesoporous microspheres, thus preventing  $\text{TiO}_2$  microspheres from collapsing after 12 h reaction. The surface of the as-obtained  $\text{TiO}_2\text{-SnO}_2$  microspheres is rough and the mesoporous structure is seen as shown in Fig. 2b; Fig. S3 and S4b (ESI<sup>†</sup>). Then  $\text{TiO}_2\text{-SnO}_2\text{@C}$  and  $\text{TiO}_2\text{-Sn@C}$  microspheres are obtained after step II and step III processes, respectively. Well-coated carbon with core-shell structure can be clearly observed in Fig. S3 (ESI<sup>†</sup>). A  $\text{TiO}_2$  matrix and a carbon shell can prevent the aggregation between Sn particles during step III. SEM images of the products at each stage are shown in Fig. S4 (ESI<sup>†</sup>).

Fig. S5a (ESI<sup>†</sup>) shows wide-angle XRD patterns of  $\text{TiO}_2\text{-SnO}_2$  and  $\text{TiO}_2\text{-Sn@C}$  microspheres. The XRD profile of the product after step I is divided into two phases, namely tetragonal anatase  $\text{TiO}_2$  (JCPDS 21-1272) and tetragonal rutile  $\text{SnO}_2$  (JCPDS 41-1445). The broad peaks indicate that this product is not well-crystallized and the crystallized size is small. After thermal reduction using carbon in step III, the final product is comprised of two parts. One is still in line with anatase  $\text{TiO}_2$ , and the other one accords well with  $\beta\text{-Sn}$  (JCPDS 86-2265). There is a small amount of  $\text{SnO}_2$  impurity existing in the final product, since it is deeply inserted into  $\text{TiO}_2$ . Small-angle XRD patterns of these two products in Fig. S5b (ESI<sup>†</sup>) confirm the mesoporous structure. In addition, the weight proportions of  $\text{TiO}_2$  and Sn are measured to be 39.1% and 37.5% based on ICP analysis, respectively. To further understand the structural properties, Raman spectra of  $\text{TiO}_2\text{-SnO}_2$  and  $\text{TiO}_2\text{-Sn@C}$  were measured (see Fig. S6, ESI<sup>†</sup>). In  $\text{TiO}_2\text{-SnO}_2$ ,  $\text{TiO}_2$  is more reflected than  $\text{SnO}_2$ , with five resolved peaks located at 143.5, 199, 395.5, 515, and 633  $\text{cm}^{-1}$ , corresponding to symmetric vibration modes of  $A_{1g} + 2B_{1g} + 3E_g$  of the tetragonal anatase phase.  $\text{SnO}_2$  has an intense peak at 633  $\text{cm}^{-1}$  and a weak peak near 515  $\text{cm}^{-1}$ , overlapping with those of anatase  $\text{TiO}_2$ , so peaks of  $\text{TiO}_2\text{-SnO}_2$  at 633  $\text{cm}^{-1}$  and 515  $\text{cm}^{-1}$  are more intense than those of  $\text{TiO}_2\text{-Sn@C}$ . Except for peaks of  $\text{TiO}_2$ ,  $\text{TiO}_2\text{-Sn@C}$  have two broad peaks at 1333 and 1575.5  $\text{cm}^{-1}$ , which are designated as disorder (D) and graphene (G) bands of carbon, respectively. The G band is associated with the allowed  $E_{2g}$  optical modes of the Brillouin zone center of the

crystalline graphite, while the D band is assigned to double-resonance excitation of phonons close to the *K*-point in the Brillouin zone. As shown in Fig. S7 (ESI<sup>†</sup>),  $\text{TiO}_2\text{-SnO}_2$  and  $\text{TiO}_2\text{-Sn@C}$  display typical type-IV isotherm curves with a representative  $H_1$ -type  $\text{N}_2$  adsorption-desorption hysteresis loop, according to IUPAC classification. This result indicates the mesoporosity structure, which can also be confirmed by BJH pore-size distributions. The BET surface area and pore volume of  $\text{TiO}_2\text{-SnO}_2$  and  $\text{TiO}_2\text{-Sn@C}$  are 125.5 and 166.6  $\text{m}^2 \text{g}^{-1}$ , and 0.294 and 0.164  $\text{cm}^3 \text{g}^{-1}$ , respectively.

CV curves of  $\text{TiO}_2\text{-Sn@C}$  at a scan rate of 0.5  $\text{mV s}^{-1}$  with cutoff voltages of 2.5–0 V (*versus*  $\text{Li}^+/\text{Li}$ ) are shown in Fig. 3a. One pair of cathodic-anodic peaks located at 1.73 and 2.15 V can be observed, relating to  $\text{Li}^+$  insertion into and extraction from the interstitial octahedral site of  $\text{TiO}_2$  reversibly, during which a two-phase reaction occurs with phase equilibrium of the Li-poor  $\text{Li}_{0.01}\text{TiO}_2$  (tetragonal) phase and the Li-rich  $\text{Li}_{0.55}\text{TiO}_2$  (orthorhombic) phase.<sup>9</sup> The cathodic peak at 0.6 V in the 1st cycle is ascribed to Sn alloying with Li, and the anodic peaks at around 0.12 and 0.54 V are assigned to the de-alloying process. A large irreversible part in the 1st cycle can be observed, mainly owing to irreversible lithium intercalation into  $\text{TiO}_2$  and amorphous carbon below 1 V, degradation of the electrolyte, and inevitable capacity loss of Sn. It is also noted that 2nd and 3rd cycles nearly overlap, indicative of good reversibility after the 1st cycle.

The cycling performances of  $\text{TiO}_2\text{-SnO}_2$  and  $\text{TiO}_2\text{-Sn@C}$  are studied by the galvanostatic method between 2.5 and 0.01 V, as shown in Fig. 3b. For comparison,  $\text{TiO}_2$  mesoporous microspheres (Fig. S2a, ESI<sup>†</sup>) and Sn@C core-shell microspheres (Fig. S2d, ESI<sup>†</sup>) are also investigated under the same conditions. At 500  $\text{mA g}^{-1}$ ,  $\text{TiO}_2$  gives discharge capacities of 750.6 and 152.2  $\text{mA h g}^{-1}$  at 1st and 200th cycles respectively. The discharge capacity of Sn@C at the 1st cycle is 970.5  $\text{mA h g}^{-1}$ , larger than that of  $\text{TiO}_2$ , whereas it drops to 137  $\text{mA h g}^{-1}$  after 200 cycles. Although the carbon shell is well-coated outside Sn microspheres, the particle size of Sn is too large. The dramatic volume change of Sn during the alloying process would make the carbon shell collapse and pulverize Sn microspheres, consequently leading to the connectivity loss of the active material and poor cyclability.  $\text{SnO}_2\text{-TiO}_2$  exhibits the largest initial discharge capacity, due to the formation of  $\text{Li}_2\text{O}$ . After 200 cycles, the capacity gradually decreases to 143.7  $\text{mA h g}^{-1}$  with poor capacity retention. When both the  $\text{TiO}_2$  matrix and the carbon shell are employed,  $\text{TiO}_2\text{-Sn@C}$  gives the best cycling performance of 246.5  $\text{mA h g}^{-1}$  at the 200th cycle. The increase in the unit cell volume of  $\text{TiO}_2$  is merely 4% from anatase to lithium titanate, so the  $\text{TiO}_2$  matrix can effectively cushion volume change and structural stress of Sn during the lithium storage process. In addition, the mesoporous structure can provide enough void space to accommodate volume expansion of Sn, and the amorphous carbon shell contributes to improved mechanical property and an enhanced buffer effect. The long-term cycling performance of  $\text{TiO}_2\text{-Sn@C}$  is displayed in Fig. 3c. Such a long cycle life has never been reported for Sn anode materials before. The reversible capacity of 206.2  $\text{mA h g}^{-1}$  can be maintained after 2000 cycles. The capacity loss in each cycle from 200 to 2000 cycles is merely 0.022  $\text{mA h g}^{-1}$ . The initial three discharge-charge curves are presented in Fig. S8 (ESI<sup>†</sup>), showing a typical sloping voltage profile, with coulombic efficiencies being 48.4%, 85.5%, and 87.3%, respectively. After  $\sim 200$  cycles,  $\text{TiO}_2\text{-Sn@C}$  is further charged and discharged at progressively higher rates for additional 200 cycles, as



**Fig. 3** (a) Cyclic voltammogram of  $\text{TiO}_2\text{-Sn@C}$  at a scan rate of  $0.5 \text{ mV s}^{-1}$  between 2.5 and 0 V, (b) cycling performances of crystallized  $\text{TiO}_2$ ,  $\text{Sn@C}$ ,  $\text{TiO}_2\text{-SnO}_2$ , and  $\text{TiO}_2\text{-Sn@C}$  at  $500 \text{ mA g}^{-1}$ , (c) long-term cycling performance of  $\text{TiO}_2\text{-Sn@C}$  at  $500 \text{ mA g}^{-1}$ , and (d) rate performance of  $\text{TiO}_2\text{-Sn@C}$ .

shown in Fig. 3d. Two kinds of carbon-based materials are also investigated. They are artificial graphite (MAG) and mesocarbon microspheres (CMS). The average capacities of MAG/CMS at 500, 1000, 3000, and 5000  $\text{mA g}^{-1}$  are 206.5/206.3, 96.6/78.5, 37.5/41.0, and 12.5/33.3  $\text{mA h g}^{-1}$ , respectively. As for  $\text{TiO}_2\text{-Sn@C}$ , they are 242.9, 213.5, 157.1, and 131.8  $\text{mA h g}^{-1}$ , much higher than those of MAG/CMS.

In summary, we have prepared mesoporous  $\text{TiO}_2\text{-Sn@C}$  core-shell microspheres by using mono-dispersed amorphous  $\text{TiO}_2$  microspheres as precursors. In this composite, Sn is encapsulated into a  $\text{TiO}_2$  mesoporous microsphere matrix, with a well-coated carbon shell. The mesoporous  $\text{TiO}_2$  matrix and the carbon shell can prevent the aggregation of Sn, buffer volume change and accommodate structural stress of Sn during electrochemical processes. The as-prepared  $\text{TiO}_2\text{-Sn@C}$  composite exhibits excellent long-term cycling stability of 2000 cycles, which has never been reported for Sn anode materials. Improved high-rate cyclability ( $131.8 \text{ mA h g}^{-1}$  at  $5000 \text{ mA g}^{-1}$ ) is also obtained, significantly better than those of typical carbon anode materials.

We are grateful for financial support from National Natural Science Foundation of China (Grants No. 21103108 and 21173148).

## Notes and references

- (a) M. R. Palacín, *Chem. Soc. Rev.*, 2009, **38**, 2565; (b) B. Scrosati and J. Garche, *J. Power Sources*, 2010, **195**, 2419.
- P. G. Bruce, B. Scrosati and J. M. Tarascon, *Angew. Chem., Int. Ed.*, 2008, **47**, 2930.
- (a) H. Shi, J. Barker, M. Y. Saidi, R. Koksang and L. Morris, *J. Power Sources*, 1997, **68**, 291; (b) D. Deng and J. Y. Lee, *J. Mater. Chem.*, 2010, **20**, 8045; (c) J. Hassoun, K. S. Lee, Y. K. Sun and B. Scrosati, *J. Am. Chem. Soc.*, 2011, **133**, 3139; (d) K. C. Hsu, C. E. Liu, P. C. Chen, C. Y. Lee and H. T. Chiu, *J. Mater. Chem.*, 2012, **22**, 21533; (e) H. Liu, R. Z. Hu, M. Q. Zeng, J. W. Liu and M. Zhu, *J. Mater. Chem.*, 2012, **22**, 8022; (f) Y. H. Xu, J. C. Guo and C. S. Wang, *J. Mater. Chem.*, 2012, **22**, 9562; (g) F. S. Ke, L. Huang, B. C. Solomon, G. Z. Wei, L. J. Xue, B. Zhang, J. T. Li, X. D. Zhou and S. G. Sun, *J. Mater. Chem.*, 2012, **22**, 17511; (h) Z. Wei, H. Mao, T. Huang and A. S. Yu, *J. Power Sources*, 2013, **223**, 50.
- M. Winter, J. O. Besenhard, M. E. Spahr and P. Novák, *Adv. Mater.*, 1998, **10**, 725.
- J. O. Besenhard, J. Yang and M. Winter, *J. Power Sources*, 1997, **68**, 87.
- (a) C. S. Wang, A. J. Appleby and F. E. Little, *J. Power Sources*, 2001, **93**, 174; (b) T. Zhang, L. J. Fu, J. Gao, Y. P. Wu, R. Holze and H. Q. Wu, *J. Power Sources*, 2007, **174**, 770.
- (a) H. Shi, J. Barker, M. Y. Saidi, R. Koksang and L. Morris, *J. Power Sources*, 1997, **68**, 291; (b) D. Deng and J. Y. Lee, *J. Mater. Chem.*, 2010, **20**, 8045; (c) J. Hassoun, K. S. Lee, Y. K. Sun and B. Scrosati, *J. Am. Chem. Soc.*, 2011, **133**, 3139; (d) K. C. Hsu, C. E. Liu, P. C. Chen, C. Y. Lee and H. T. Chiu, *J. Mater. Chem.*, 2012, **22**, 21533; (e) H. Liu, R. Z. Hu, M. Q. Zeng, J. W. Liu and M. Zhu, *J. Mater. Chem.*, 2012, **22**, 8022; (f) Y. H. Xu, J. C. Guo and C. S. Wang, *J. Mater. Chem.*, 2012, **22**, 9562; (g) G. X. Wang, B. Wang, X. L. Wang, J. S. Park, S. X. Dou, H. Ahn and K. Kim, *J. Mater. Chem.*, 2009, **19**, 8378.
- (a) T. Ohzuku, T. Kodama and T. Hirai, *J. Power Sources*, 1985, **14**, 153; (b) J. S. Chen and X. W. Lou, *Electrochem. Commun.*, 2009, **11**, 2232; (c) D. Deng, M. G. Kim, J. Y. Lee and J. Cho, *Energy Environ. Sci.*, 2009, **2**, 818; (d) S. J. Ding, J. S. Chen, D. Y. Luan, F. Y. C. Boey, S. Madhavi and X. W. Lou, *Chem. Commun.*, 2011, **47**, 5780; (e) J. F. Lei, W. S. Li, X. P. Li and E. J. Cairns, *J. Mater. Chem.*, 2012, **22**, 22022; (f) X. M. Wu, S. C. Zhang, L. L. Wang, Z. J. Du, H. Fang, Y. H. Ling and Z. H. Huang, *J. Mater. Chem.*, 2012, **22**, 11151.
- J. Z. Chen, L. Yang and Y. F. Tang, *J. Power Sources*, 2010, **195**, 6893.